CHEMISTRY OF MATERIALS

Article

pubs.acs.org/cm

Metal Distributions, Efficient n-Type Doping, and Evidence for in-Gap States in $TiNiM_ySn$ (M = Co, Ni, Cu) half-Heusler Nanocomposites

Ruth A. Downie,[†] Ronald I. Smith,[‡] Donald A. MacLaren,[§] and Jan-Willem G. Bos*[,†]

[†]Institute of Chemical Sciences and Centre for Advanced Energy Storage and Recovery, School of Engineering and Physical Sciences, Heriot-Watt University, Edinburgh EH14 4AS, United Kingdom

[‡]ISIS Facility, Rutherford Appleton Laboratory, Harwell Oxford, Didcot OX11 0QX, United Kingdom

[§]SUPA, School of Physics and Astronomy, University of Glasgow, Glasgow G12 8QQ, United Kingdom

Supporting Information

ABSTRACT: $XNi_{1+y}Sn$ nanocomposites consisting of a XNiSn half-Heusler (HH) matrix with segregated XNi_2Sn Full Heusler (FH) inclusions promise improvements in thermoelectric efficiencies. We extend recent research by reporting on $TiNiM_ySn$ ($0 \le y \le 1$) nanocomposites with M = Co ($3d^9$), Ni ($3d^{10}$) and Cu ($3d^{10}4s^1$). Neutron powder diffraction reveals that the Ni and Cu series produce a matrix of TiNiSn with nanosegregated $TiNi_2Sn$ and $TiNi_{1+d}Cu_{1-d}Sn$, respectively. For the Co series, the Co inserts into both phases to obtain a $TiNi_{1-y}Co_ySn$ matrix with nanosegregated $TiNi_{2-y}Co_ySn$. Systematic changes in Seebeck coefficient (S) and electrical resistivity (ρ) are observed in all three series. For M = Ni, changes in S and ρ are attributed to in-gap states arising from the nanosegregation. The M = Co composites show a complex interplay between the hole doped $TiNi_{1-y}Co_ySn$ matrix and similar in-gap states, where the p- to n-type transition temperature increases but the maximum S remains unchanged at +30 μV K^{-1}. The $4s^1$ electron for M = Cu is delocalized in the HH matrix, leading to metal-like $\rho(T)$ and up to 100% improved thermoelectric power factors compared to TiNiSn (S^2/ρ = 2 mW m^{-1} K^{-2} at 600−700 K for y = 0.025). These results broaden the range of segregated FH phases that could be used to enhance HH thermoelectric performance.

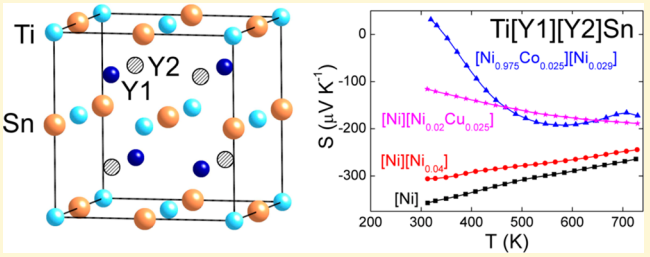

INTRODUCTION

Thermoelectric waste heat recovery is widely considered to be an important component of a sustainable energy future.[1−3] Half Heusler alloys (HHs) have been considered as candidate thermoelectric materials since the 1990s but are undergoing a renaissance due to improvements brought by introducing nanostructuring.[4−6] These include samples with reduced grain sizes (e.g., those that have undergone mechanical milling and spark plasma sintering, SPS) as well as Ni-rich $XNi_{1+y}Sn$ nanocomposites that phase segregate into a HH matrix with Full Heusler (FH) inclusions, typically using X = Ti, Zr or Hf.[5−21] Some of these nanocomposites have been reported to have enhanced thermoelectric power factors, given by S^2/ρ, because of an increase in the Seebeck coefficient, S, without the usual accompanying increase of electrical resistivity, ρ.[10,18,19] The improved ρ has been linked to a filtering of low energy carriers by FH nanoinclusions, which create potential barriers within the composite.[10] The inclusions also strongly reduce the lattice thermal conductivity, κ_{lat}, and for $TiNi_{1+y}Sn$ in particular, large increases in the figure of merit, $ZT = S^2T/\kappa\rho$, have been reported, yielding ZT = 0.6−0.7 for $y \le 0.15$ in comparison to ZT = 0.2−0.3 for y = 0.[12,14,17,20,22] Here, κ is the sum of κ_{lat} and the electronic thermal conductivity, κ_{el}, and T is the absolute temperature. These results are of particular interest as they avoid the use of rare and expensive elements such as Zr and Hf, but the nature of the phase segregation is critical and depends sensitively on the synthesis protocol.[5,6] For example, during arc- or induction melting of TiNiSn, $TiNi_2Sn$ crystallizes first upon cooling, then slowly reacts with Ti−Sn binaries and elemental Sn to form the target HH composition.[6] Non-stoichiometric Ni content is therefore inherent to these syntheses. Theoretical studies systematically indicate instability of the HH structure toward nonstoichiometry with any excess Ni segregating into FH domains rather than distributing statistically throughout the material.[23−27] The experimental and theoretical phase diagrams also report TiNiSn as a line phase.[20,28,29] Electron microscopy has revealed a wide variety of segregated FHs with length scales from a few unit cells to macroscopically segregated phases.[9,10,12,14−16,18−20] In contrast to atomic substitutions, whose impact on diffraction data is well-established, segregated phases can manifest themselves in different ways depending on their size and number densities. A statistical distribution of excess metal within a matrix results in a uniform tensile strain, leading to a shift of the Bragg peaks toward higher d-spacing without peak broadening. At a low density of nanoinclusions, most of the matrix is unaffected and

Received: December 12, 2014
Revised: March 10, 2015
Published: March 11, 2015

DOI: 10.1021/cm5045682
Chem. Mater. 2015, 27, 2449−2459

so no changes in Bragg position are expected, although microstrain around and within the inclusions may result in peak broadening since the matrix's lattice parameter is modulated. At a high density of nanoinclusions, simultaneous peak shifts and microstrain broadening are expected, since the majority of the matrix is now affected, as for example observed in the $AgSbTe_2$−PbTe (LAST) phases.[30] Large inclusions above 50 nm in diameter can occur and at even quite low dopant concentrations would be readily observed: for example, if 5% excess metal in TiNiSn were contained in 50 nm diameter spheres, then their number density would be 1×10^{15} cm^{-3} and they would manifest as distinct Bragg peaks well-separated from the HH matrix.

Here, we report on the synthesis, structural, and thermoelectric characterization of $TiNiM_ySn$ nanocomposites that are expected to segregate into a TiNiSn HH matrix with Ti(NiM)Sn FH inclusions. The excess metals M = Co ($3d^9$), Ni ($3d^{10}$), and Cu ($3d^{10}4s^1$) were chosen to afford a systematic variation of the electronic configuration and orbital energies. In addition, we report on the nominally Ni-deficient $TiNi_{1-z}Sn$ ($0.01 \leq z \leq 0.5$) series. As discussed, the M = Ni composites have already attracted significant interest, while $ZrNiCo_ySn$ composites have been the subject of at least two papers.[31,32] These samples were initially assumed to contain statistically distributed excess Co atoms on the normally vacant Y2 site of the HH structure (see below)[31] but the Y2 occupation has recently been shown to be ordered, producing 2−7 nm wide segregated Co-rich FH stripes.[32] In contrast, the structural analysis presented here demonstrates that for $TiNiCo_ySn$, substitution of Co for Ni occurs in the matrix and this forces segregation of $Ti(Ni_{2-y}Co_y)Sn$. To the best of our knowledge, there is no previous work exploiting Ti(NiCu)Sn inclusions and we show them to produce substantial improvement in thermoelectric performance. Finally, our samples were prepared using solid state reactions which do not proceed via the melt and this is expected to change the nature of phase segregation and nanostructuring compared to, for example, arc- or induction melting. No post synthesis densification was used and the three reported $TiNiM_ySn$ composite series therefore serve as a useful benchmark for more heavily processed samples in the literature.

EXPERIMENTAL SECTION

Polycrystalline $TiNiM_ySn$ samples with M = Co, Ni, and Cu and $0 \leq y \leq 1$ were prepared on a 3 g scale using standard solid state reactions. Powders of elemental starting materials (Alfa Aesar; Ti, 325 mesh; Ni, 120 mesh; Co, 1.6 μm, Cu, 625 mesh; Sn, 325 mesh; ≥ 99.8% purity) were weighed out in stoichiometric quantities and homogenized using a mortar and pestle. Pellets (13 mm diameter) were cold-pressed using a 10 ton press for 1−2 min and wrapped in Ta foil before being vacuum sealed in quartz tubes. The Ta foil (0.025 mm thickness, Sigma-Aldrich) was rolled into a cylinder with the ends folded twice and clamped using pliers, leading to a tight seal. The samples were annealed for an initial 24 h at 900 °C, and subsequently reground to ensure homogeneity, pressed during 3−5 min, then annealed for a further 2 weeks at 900 °C. In the first step, the heating rate was 10 °C/min and the samples were cooled at the natural rate of the furnace. At the end of the 2 week heating period the samples were air quenched from 900 °C. The pellets remained intact during all synthesis steps. No metal oxide impurities were observed in diffraction or in electron microscopy. The Ni deficient $TiNi_{1-z}Sn$ ($0 \leq z \leq 0.5$) samples were prepared on the same scale and using the same procedure. Neutron powder diffraction (NPD) data were collected on all samples on the recently upgraded Polaris instrument at the ISIS facility, Rutherford Appleton Laboratory, UK. Data were collected from ∼2 g of material up to a total of 200 μAh proton beam current, corresponding to ∼2 h counting time. The atomic distributions were determined using Rietveld analysis of this data using the GSAS and EXPGUI suite of programs.[33,34] The neutron scattering lengths are $b_{Ti} = -3.4$ fm, $b_{Ni} = 10.3$ fm, $b_{Co} = 2.49$ fm, $b_{Cu} = 7.72$ fm, and $b_{Sn} = 6.2$ fm and thus afford a good contrast between the constituent elements. SEM analysis was carried out using a Quanta 650 FEG ESEM operated at 20 kV and equipped with an Oxford Instruments X-max 150^N detector with AZtec software for energy dispersive X-ray spectroscopy (EDX) mapping. Transmission electron microscopy (TEM) and Scanning TEM were performed on a JEOL ARM200cF equipped with a cold field-emission gun operating at 200 kV. The instrument is equipped with a Bruker X-Flash EDX detector and Gatan 965 Quantum ER spectrometer for Electron Energy Loss Spectroscopy (EELS). Cross sections for TEM were milled directly from compressed pellets using an FEI Nova Nanolab Focused Ion Beam system: we find such samples to be more representative of typical bulk morphology than imaging the smallest powders of a ground sample. The temperature dependence of the Seebeck coefficient and electrical resistivity were measured on a Linseis LSR-3 instrument. The densities of samples suitable for electrical characterization were all of the order of 80% of the crystallographic density, as calculated from the mass and dimensions of the bars used for the transport measurements. $TiNiM_ySn$ (M = Co, Cu) samples with $y \geq 0.1$ formed as brittle pellets unsuitable for electrical characterization.

RESULTS

Crystal Structure. The TiNiSn structure (space group $F\bar{4}3m$, inset to Figure 1) can be described as a cubic close packed Sn arrangement (Wyckoff position 4*b*) that contains Ti on the octahedral site (4*a*) and Ni on half of the tetrahedral sites (4*c*, referred to as the Y1 site here). This leaves half the tetrahedral sites empty (4*d*, herein Y2). The FH structure is similar but has both the Y1 and Y2 sites filled with a statistical distribution of Ni/M atoms (space group $Fm\bar{3}m$; Ti, 4*a*; Ni/M, 8*c*; Sn, 4*b*). The X-ray diffraction patterns for all prepared $TiNiM_ySn$ samples are given in Figure S1 in the Supporting Information, whereas the lattice parameters for the HH and FH phases are given in Table 1 (M = Ni; $0 \leq y \leq 1$) and Table 2 (M = Co, Cu; $y \leq 0.075$), and Table S1 in the Supporting Information (M = Co, Cu; $y \geq 0.1$).

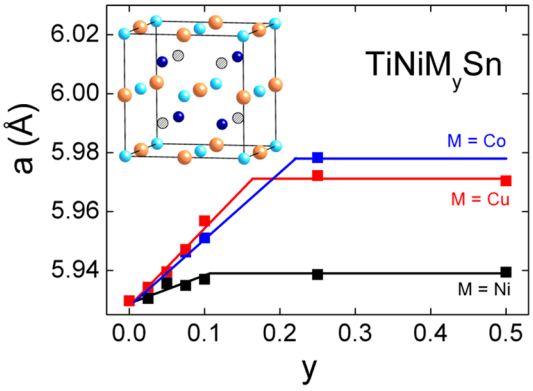

Figure 1. Lattice parameters of the HH phase for the $TiNiM_ySn$ (M = Co, Ni and Cu) series. The inset shows the HH unit cell with Ti (pale blue), Ni (dark blue) and Sn (gold) sublattices. Ni occupies the Y1 sites. The other tetrahedral sites (Y2), indicated as hatched spheres, are occupied in the FH structure.

$TiNi_{1+y}Sn$ ($0 \leq y \leq 1$). This series spans the TiNiSn-$TiNi_2Sn$ pseudobinary. The evolution of the HH lattice parameter is shown in Figure 1 (black trace) and reveals a gradual increase up to $y = 0.1$, beyond which no further change is observed. This

DOI: 10.1021/cm5045682
Chem. Mater. 2015, 27, 2449−2459

Table 1. Lattice Parameters (a), Weight Percentages, Fractional Occupancies, Temperature Displacement Factors (U_{iso}/Å^2), and Refined Compositions for the HH and Distinct FH Phases That Were Used to Fit the Polaris Neutron Powder Diffraction for the $TiNi_{1+y}Sn$ series ($0 \le y \le 1$); Fitted Band Gaps for Carrier Transport Are Also Given[a]

y		0	0.025	0.05	0.075	0.1	0.25	0.5	1
					Half-Heusler				
a (Å)		5.9297(1)	5.9305(1)	5.9355(1)	5.9349(1)	5.9371(1)	5.9386(1)	5.9394(1)	
wt %		100	98.94(6)	95.5(2)	94.8(2)	92.5(1)	69.1(1)	35.4(1)	
Ti (4a)	Occ	1	1	1	1	1	1	1	
	U_{iso}	0.00494(7)	0.00447(7)	0.00436(7)	0.00439(7)	0.00435(7)	0.00438(9)	0.0041(2)	
Ni (4c)	Occ	1	1	1	1	1	1	1	
	U_{iso}	0.00499(5)	0.00495(5)	0.00514(5)	0.00511(5)	0.00539(5)	0.00569(6)	0.0059(1)	
Ni (4d)	Occ	0.021(1)	0.041(1)	0.056(1)	0.060(1)	0.071(1)	0.078(1)	0.080(2)	
	U_{iso}	0.00499(5)	0.00495(5)	0.00514(5)	0.00511(5)	0.00539(5)	0.00569(6)	0.0059(1)	
Sn (4b)	Occ	1	1	1	1	1	1	1	
	U_{iso}	0.00405(6)	0.00399(6)	0.0408(5)	0.00406(5)	0.00418(5)	0.00432(7)	0.0045(1)	
refined compositions		$TiNi_{1.021(1)}Sn$	$TiNi_{1.041(1)}Sn$	$TiNi_{1.056(1)}Sn$	$TiNi_{1.060(1)}Sn$	$TiNi_{1.071(1)}Sn$	$TiNi_{1.078(1)}Sn$	$TiNi_{1.080(2)}Sn$	
					Full-Heusler				
a (Å)			6.0691(4)	6.0756(3)	6.0764(2)	6.0767(1)	6.0750(1)	6.0744(1)	6.0955(1)
wt %			1.06(6)	4.5(2)	5.2(2)	7.5(1)	30.9(1)	64.6(1)[b]	94.40(6)[b]
Ti (4a)	Occ		1	1	1	1	1	1	1
	U_{iso}		0.001	0.011(1)	0.008(1)	0.0084(3)	0.0070(2)	0.0072(1)	0.0054(1)
Ni (8c)	Occ		0.80(3)	0.84(2)	0.93(1)	0.92(1)	0.900(3)	0.900(2)	0.991(2)
	U_{iso}		0.001	0.0105(7)	0.0131(6)	0.0123(3)	0.0118(1)	0.01192(7)	
Sn (4b)	Occ		1	1	1	1	1	1	1
	U_{iso}		0.001	0.009(1)	0.009(1)	0.0085(3)	0.0085(2)	0.0084(1)	0.00705(9)
refined compositions			$TiNi_{1.60(4)}Sn$	$TiNi_{1.68(3)}Sn$	$TiNi_{1.86(1)}Sn$	$TiNi_{1.84(1)}Sn$	$TiNi_{1.800(4)}Sn$	$TiNi_{1.800(3)}Sn$	$TiNi_{1.982(4)}Sn$
E_g (eV)		0.148(2)	0.132(2)	0.112(2)	0.106(2)	0.112(2)	0.084(2)		
average composition		$TiNi_{1.021(1)}Sn$	$TiNi_{1.05(2)}Sn$	$TiNi_{1.08(1)}Sn$	$TiNi_{1.10(1)}Sn$	$TiNi_{1.12(1)}Sn$	$TiNi_{1.270(5)}Sn$	$TiNi_{1.509(4)}Sn$	$TiNi_{1.982(4)}Sn$
$\chi^2_{(Rietveld)}$ /$\chi^2_{(Le\ Bail)}$		1.04	1.19	1.15	1.13	1.12	1.16	1.21	2.14
wR_p (%)	bank 1	3.13	2.32	2.23	2.14	2.08	2.46	3.66	2.50
	bank 2	1.95	1.88	2.04	1.88	1.88	2.62	2.07	2.51
	bank 3	2.11	2.84	3.07	2.51	2.58	2.69	2.47	2.99
R_p (%)	bank 1	3.55	2.88	2.53	2.55	2.35	3.59	5.74	3.22
	bank 2	3.22	3.57	3.81	3.49	3.48	4.09	3.32	3.67
	bank 3	3.59	3.57	3.64	3.22	3.18	3.24	2.94	3.33

[a]Half-Heusler space group = $F\bar{4}3m$ − 4a: (0,0,0), 4b: (1/2, 1/2. 1/2), 4c: (1/4, 1/4, 1/4), 4d: (3/4, 3/4, 3/4). Heusler space group = $Fm\bar{3}m$ − 4a: (0,0,0), 4b: (1/2, 1/2. 1/2), 8c: (1/4, 1/4, 1/4). [b]Samples contain Ni3Sn2 impurities.

is in keeping with the literature,[20] which suggests that up to 10% Ni can be accommodated. However, the NPD data reveal that even for $y \le 0.1$, distinct FH peaks occur, revealing that at least part of the excess Ni has segregated into FH phases with a size large enough to lead to coherent diffraction. The weight fractions of this distinct FH phase increase from 1 wt % for y = 0.025 to 7.5 wt % for y = 0.1 (Table 1). For $y \ge 0.25$, large quantities of distinct FH are evident (e.g., 31 wt % for y = 0.25, Table 1). The evolution of the HH (422) reflection and the full-width at half maximum are shown in Figure 2a, b and reveal an invariant line shape across the range. This reflection was chosen due to the better resolution at higher angles, enabling subtle changes in peak position and width to be observed,[35] although similar trends will occur in peaks at lower angles. These samples therefore show an expanded HH lattice without appreciable peak broadening, which suggests either a statistical distribution of the excess Ni or a large number of small inclusions that exert uniform tensile strain on the surrounding HH lattice. Rietveld analysis of neutron powder diffraction data was used to obtain the experimental compositions of the HH and distinct FH phases that are observed for the $TiNi_{1+y}Sn$ series. The data were fitted using a metal-rich HH phase, which represents an average of the matrix and any nanosegregated FH phase, and a distinct FH phase with an independent lattice parameter. Refinement of the HH Y1 and Y2 site occupancies yields the composition and amount of the HH matrix and the nanosegregated FH phase.[17,25] The results of the Rietveld fits for the $TiNi_{1+y}Sn$ series are summarized in Table 1. A representative Rietveld fit for $TiNi_{1.05}Sn$ is shown in Figure 3, whereas fits to all other compositions can be found in Figure S2 in the Supporting Information. Focusing first on the HH phase: the Rietveld fitting demonstrates that the y = 0 sample has a 2% Ni occupancy of the Y2 site (Table 1) and that ∼2% nanosegregated $TiNi_2Sn$ is therefore present in this sample. The χ^2 value improves by 10−20% for this series upon partial occupation of the Y2 site. The Y2 site occupancy gradually increases to a maximum of 7−8% for y = 0.1−0.5, which is somewhat lower than inferred from the lattice parameters (Figure 1), but this is not unexpected given the presence of the distinct FH phase. The distinct FH phases also show an increase in lattice parameter and for y = 1 the expected $TiNi_2Sn$ composition is obtained from refinement of the site-occupancies (Table 1). For smaller y values, the Y sites of FH phases are poor in Ni with experimental composition $TiNi_{2-x}Sn$ ($0 \le x \le 0.4$; Table 1). Ni deficiency in the FH structure has been observed experimentally,[17,29] and is

DOI: 10.1021/cm5045682
Chem. Mater. 2015, 27, 2449−2459

Table 2. Lattice Parameters (a), Fractional Occupancies, Temperature Displacement Factors (U_{iso}/Å^2), and Refined Compositions for the HH Phases Used to Fit the Polaris Neutron Powder Diffraction Data Collected on the TiNiCo$_y$Sn and TiNiCu$_y$Sn Series ($y \leq 0.075$); fitted Band Gaps for Carrier Transport Are Also Given

		M = Co			M = Cu		
y		0.025	0.05	0.075	0.025	0.05	0.075
a (Å)		5.9309(1)	5.9368(1)	5.9462(1)	5.9343(1)	5.9395(1)	5.9471(1)
Ti (4a)	Occ	1	1	1	1	1	1
	U_{iso}	0.00473(8)	0.00453(7)	0.00484(7)	0.00468(8)	0.00465(8)	0.00500(8)
Ni (4c)	Occ	0.975	0.95	0.925	1	1	1
	U_{iso}	0.00478(5)	0.00507(5)	0.00571(5)	0.00493(5)	0.00492(5)	0.00548(5)
Co (4c)	Occ	0.025	0.05	0.075			
	U_{iso}	0.00478(5)	0.00507(5)	0.00571(5)			
Ni (4d)	Occ	0.029(1)	0.065(1)	0.099(1)	0.020	0.020	0.020
	U_{iso}	0.00481(5)	0.00507(5)	0.00571(5)	0.00493(5)	0.00492(5)	0.00548(5)
Cu (4d)	Occ				0.026(1)	0.054(1)	0.076(1)
	U_{iso}				0.00493(5)	0.00492(5)	0.00548(5)
Sn (4b)	Occ	1	1	1	1	1	1
	U_{iso}	0.00404(6)	0.00412(5)	0.00473(5)	0.00409(6)	0.00406(6)	0.00453(6)
refined composition		$TiNi_{1.004(1)}Co_{0.025}Sn$	$TiNi_{1.015(1)}Co_{0.05}Sn$	$TiNi_{1.024(1)}Co_{0.075}Sn$	$TiNi_{1.020}Cu_{0.026(1)}Sn$	$TiNi_{1.020}Cu_{0.054(0)}Sn$	$TiNi_{1.020}Cu_{0.076(1)}Sn$
E_g (eV) > 600 K		0.53(1)	0.52(2)	0.42(2)			
E_g (eV) < 600 K		0.23(2)	0.062(6)	0.010(2)			
$\chi^2_{(Rietveld)}$ /$\chi^2_{(Le\ Bail)}$		1.02	1.01	1.00	0.99	0.99	0.99
wR_p (%)	bank 1	2.69	2.43	2.45	2.40	2.32	2.43
	bank 2	2.10	1.94	2.10	2.03	1.92	1.95
	bank 3	3.26	2.93	3.43	3.23	2.66	3.21
R_p (%)	bank 1	3.09	2.81	2.92	2.86	2.76	2.93
	bank 2	3.51	3.61	3.68	3.72	3.55	3.58
	bank 3	3.75	3.75	3.91	3.79	3.61	3.64

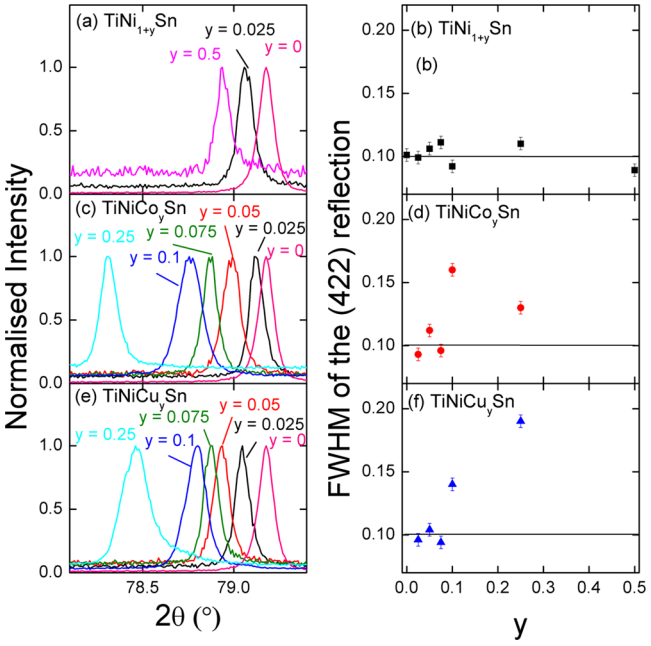

Figure 2. Close-up and full width at half maximum of the HH (422) XRD reflection for the (a, b) TiNi$_{1+y}$Sn, (c, d) TiNiCo$_y$Sn, and (e, f) TiNiCu$_y$Sn series.

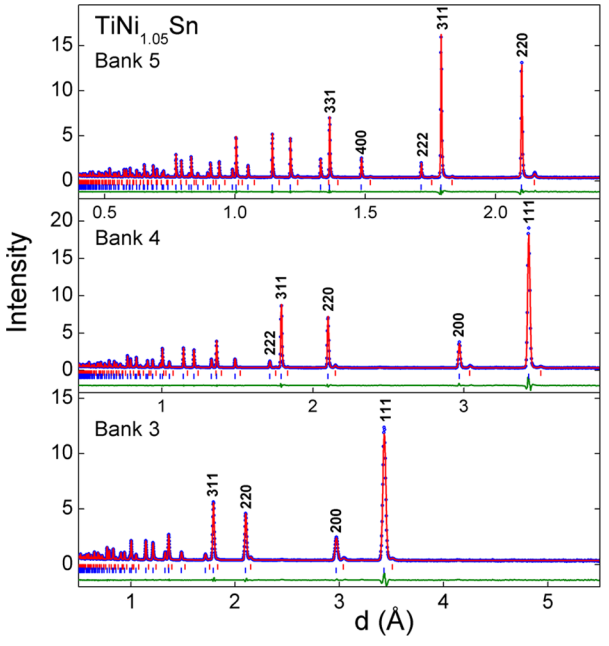

Figure 3. Observed (blue circles), calculated (red line), and difference neutron powder diffraction Rietveld profiles for the TiNi$_{1.05}$Sn sample, measured on three banks of NPD detectors (top to bottom panels). The Bragg markers correspond to the HH phase $TiNi_{1.056(1)}Sn$ (bottom) and a 4 wt % FH phase ($TiNi_{1.68(1)}Sn$, top).

reproduced by computational studies that suggest that the vacancies repel and do not cluster.[23,26] Non-stoichiometry and metal inversion are unfavorable in covalent HHs but carry a smaller energy penalty in the metallic FH structure.[36] The weighted average of the HH and distinct FH compositions is in good agreement with the nominal composition, with the consistent observation of an additional 2% Ni (Table 1). The presence of this unintentional Ni excess is in keeping with the observation of Ti- and Sn-rich regions in EDX elemental mapping for the y = 0 sample (Figure S3 in the Supporting Information) and with the frequent observation of Ti_5Sn_3 and Ti_6Sn_5 impurities in the literature.[6,17,20,37] This suggests an

DOI: 10.1021/cm5045682
Chem. Mater. 2015, 27, 2449−2459

incomplete reaction which may be caused by the sublimation of small amounts of Sn, which could force the formation of Ti-rich Sn binaries and result in a small excess of Ni within the HH structure. To summarize, analysis of the diffraction data reveals that the excess Ni in $TiNi_{1+y}Sn$ is divided over a metal-rich, potentially nanosegregated HH and a distinct FH phase. Inspection of the fitted wt % and compositions in Table 1 reveals that for $y \leq 0.075$, most of the excess Ni is associated with the HH phase, while for $y = 0.1$ the amount of Ni in the distinct FH phase exceeds that of the HH. For $y \geq 0.25$ a clear majority of the excess Ni is found in the distinct FH phase.

$TiNiCo_ySn$. This series spans the TiNiSn−Ti(NiCo)Sn pseudobinary. As above, the HH lattice parameter increases gradually up to $y = 0.1$ (Figure 1, blue trace). Linear extrapolation of the lattice parameter for $y \leq 0.1$ suggests an estimated solubility limit near y = 0.2, indicated by the break-point in Figure 1. Inspection of the X-ray line shapes in Figure 2c, d reveals an invariant line shape for $y \leq 0.075$ and peak broadening for the $y = 0.1$ sample. The initial expansion of the HH matrix without peak broadening again suggests either uniform distribution or the presence of a large number of small inclusions, similar to $TiNi_{1+y}Sn$, while the peak broadening suggests that the nanosegregated domains have reached a critical size. NPD and XRD reveal that these samples do not contain any distinct FH phase for $y \leq 0.075$ and Rietveld analysis indeed confirms that all excess metal is located in the HH phase (see below). For $y \geq 0.25$, strong distinct FH reflections are observed in XRD, demonstrating that part of the excess metal is now located in a distinct FH phase (Figure S1b in the Supporting Information). The results of the Rietveld analysis of neutron powder diffraction data on the samples with sharp XRD line shapes ($y \leq 0.075$) is summarized in Table 2. Excellent goodness-of-fit statistics, close to those from Lebail fits, were obtained. The presence of both Ni and Co means an unrestricted refinement of the HH composition is not possible, as both the elemental ratio and the Y2 site occupancy can be varied. Trial fits with Co on the Y2 site yielded unrealistically large occupancies, suggesting that Ni was present. The best fits were obtained with substitution of Co on the Y1 site (which therefore contains a mix of Ni and Co) and displacement of Ni to the Y2 site. Refinement of the Y2 site occupancy revealed an increase from 0.029(1) for $y = 0.025$ to 0.099(1) for $y = 0.075$, resulting in an overall 0.5−2.5% Ni excess over the nominal values, as summarized in Table 2. The Rietveld analysis therefore demonstrates that for $y \leq 0.075$ these samples consist of a $TiNi_{1-y}Co_ySn$ matrix and nanosegregated $TiNi_{2-y}Co_ySn$ inclusions without any distinct FH phases present.

$TiNiCu_ySn$. This series spans the TiNiSn−Ti(NiCu)Sn pseudobinary. The HH lattice parameters follow those of the Co series closely (Figure 1, red trace). Linear extrapolation suggests a similar upper limit near $y = 0.15$, and from Figure 2e, f it is evident that peak broadening becomes a factor for $y = 0.1$ onwards. For $y \leq 0.075$, the lack of peak broadening and similar widths compared to the other series once again suggests either uniform distribution of the excess metal or the presence of large number densities of nanoscale inclusions. The broadening for $y \geq 0.1$ is similar to that observed in the Co series, suggesting that the inclusions are expanding in size. For $y \geq 0.25$ large amounts of distinct FH phases are observed in XRD (Figure S1c in the Supporting Information). NPD confirms that the $y \leq 0.075$ samples only contain a HH phase with no evidence for distinct FH reflections and these data were therefore fitted using a single metal-rich HH phase. The best Rietveld fits were obtained with Cu inserted on the Y2 site. However, free refinement of the Y2 site occupancies led to unphysical values for the Cu content, again suggesting the presence of Ni. The addition of 2% Ni onto the Y2 site brings the refined Cu content to within a few standard deviations of the nominal values (Table 2). This series therefore consists of a TiNiSn matrix with Ni and Cu-rich nanosegregated FH regions. The average compositions of the FH phases were calculated to be $Ti(Ni_{1.44}Cu_{0.56})Sn$ ($y = 0.025$), $Ti(Ni_{1.27}Cu_{0.73})Sn$ ($y = 0.05$), and $Ti(Ni_{1.2}Cu_{0.8})Sn$ ($y = 0.075$), where the deviation from the ideal Ti(NiCu)Sn composition is due to the presence of the 2% additional Ni.

$TiNi_{1-z}Sn$ ($0.01 \leq z \leq 0.5$). This series was prepared to investigate the possibility of Ni-poor half Heuslers, which proved impossible, and the results are therefore only discussed briefly. Rietveld fits to representative neutron powder diffraction patterns for the z = 0.01 and 0.5 samples are presented in Figure S4 in the Supporting Information, whereas crystallographic data for all samples are presented in Table S2 in the Supporting Information. All compositions contained a HH phase with increasing amounts of hexagonal and orthorhombic Ti_6Sn_5 impurity phases as z was increased. Refinement of the site occupancies of the HH phase demonstrates that for the highest z-values (most Ni deficient starting composition) almost stoichiometric TiNiSn can be obtained (e.g., $TiNi_{1.003(1)}Sn$ for $z = 0.3$) but within a rather impure sample. The temperature dependence of the Seebeck coefficient and the electrical resistivity are shown in Figure S5 in the Supporting Information. The observed $S(T)$ and $\rho(T)$ are similar to that of TiNiSn for low z-values but rapidly become metallic as the amount of impurities increases.

Lattice Parameter and Y2 Site Occupancy. Figure 4 consolidates the crystallographic information in the form of a plot of lattice parameter against refined Y2 site occupancy for all investigated composites. This reveals a near universal linear relation between lattice parameter and total Y2 site occupancy or, equivalently, the amount of nanosegregated FH phase. The straight line fit suggests an ideal lattice parameter of a = 5.9214(5) Å for TiNiSn and an extrapolated a = 6.16(1) Å for the FH phase. This is substantially larger than the experimental values of a = 6.10 Å, 6.09, and 6.12 Å for M = Ni, Co, and Cu, respectively (see Table S1 in the Supporting Information). In case of statistically distributed dopants Vegard's law may be expected to hold but extrapolation of the HH lattice parameter

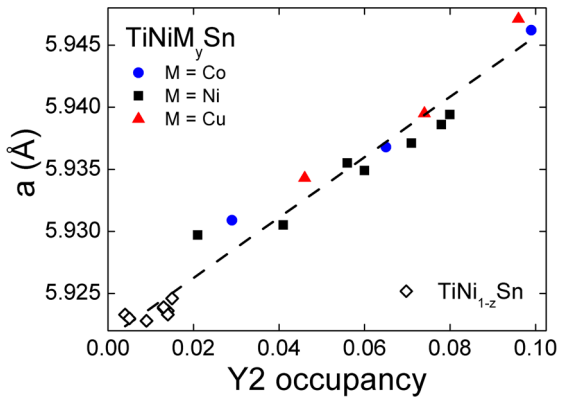

Figure 4. Universal plot showing the HH lattice parameters for the $TiNiM_ySn$ (M = Co, Ni, and Cu) and nominally Ni-deficient $TiNi_{1-z}Sn$ samples as a function of the refined Y2-site occupancy.

DOI: 10.1021/cm5045682
Chem. Mater. 2015, 27, 2449−2459

leads to a strong overestimate for TiNiMSn (M = Co, Ni and Cu). This suggests that the HH host material is incurring significant tensile strain, beyond that expected from atomic dopants, and in keeping with the postulated presence of large amounts of nanosegregated FH inclusions.

Electron Microscopy. Analysis of the XRD and NPD data has revealed that all $TiNiM_ySn$ samples contain a metal-rich, potentially nanosegregated, HH phase, while distinct FH phases are also observed. The $TiNi_{1.05}Sn$ sample contains 95.5 wt % metal-rich HH phase ($TiNi_{1.056(1)}Sn$) and 5 wt % of a distinct FH phase ($TiNi_{1.68(1)}Sn$), and was selected as a representative example for investigation of the distribution of the excess metal. Low magnification scanning transmission electron microscopy (STEM) images of a cross-section of a $TiNi_{1.05}Sn$ pellet are presented in Figure 5. The material straddles several grains, with the grain boundaries visible as white bands in dark field, such as those indicated at position 1.

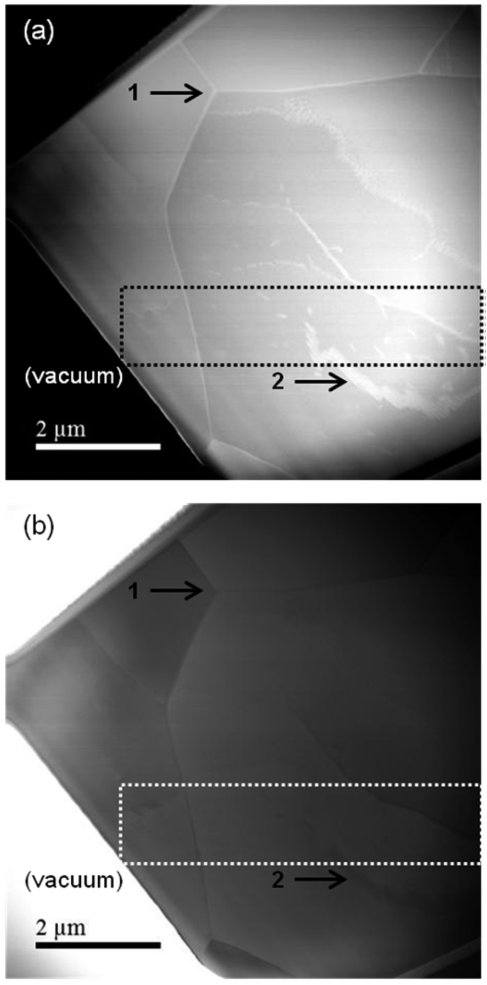

Figure 5. (a) Dark-field and (b) bright-field STEM images of a wide-area cross-section through a $TiNi_{1.05}Sn$ pellet. In both images, the contrast is largely uniform, and there is no evidence for clear phase segregation or the formation of inclusions. Continuous bright lines in the dark field image, such as the triple boundary indicated at position 1, are the boundaries and junctions between separate grains, which have fused. Weaker features such as those indicated at position 2 are consistent with dislocation networks. The rectangular section is prepared by FIB techniques and the thin protective layer of Pt that was deposited prior to ion milling is just visible to the lower right. The dotted lines indicate the region used for EDX spectrum imaging.

Grains were identified by a clear change in crystal orientation that was noted in electron diffraction (not shown). The grains have clearly fused together and there are no obvious cavities or voids, suggesting successful densification in this region of the pellet. Contrast in dark field STEM (Figure 5a) is dominated by variations in elemental composition and strain; in previous studies,[10,12] the formation of inclusions has given rise to clear dark-field contrast variations across the material. Here, the material lacks notable contrast variations on the 10 nm to 1 μm length scale, apart from the grain boundaries noted above (position 1) and for occasional features that are consistent with dislocation networks, such as the contrast indicated at position 2. The formation of dislocation networks might be expected to arise from mechanical processing of the material. Variations in composition across the cross-section were first assessed by EDX, and summarized elemental profiles collected from the box illustrated in Figure 5 are presented in Figure 6. Note that

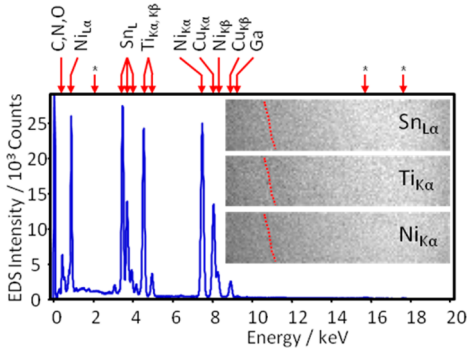

Figure 6. EDX spectrum imaging analysis of the region indicated in Figure 5. The main plot indicates the summed spectra across the region, with main features annotated above. The Cu signal is attributed to secondary scattering from the sample mount; C, N, O, and Ga are consistent with surface contamination of FIB-prepared samples. The asterisks indicate a small quantity (~1%) of Zr contamination uniformly distributed across the sample. Inset: spatial distribution of Sn, Ti, and Ni EDS counts collected across the region, measured in 1 nm^2 pixels. The dotted red line in each panel indicates the approximate location of the grain boundary seen in Figure 5

the area analyzed straddles both a region of dislocation networks and a grain boundary, the latter of which is indicated by a red dashed line in the three subpanels of Figure 6. The integrated EDX spectrum is dominated by Ti, Ni, and Sn peaks, alongside a Cu peak that arises from scattering from the sample mount, C,N and O that are ascribed to surface contamination, and a ~1 at % Zr impurity. Using the integrated Ti Kα, Ni Kα, Sr Kα, and Sn L counts, routines with the Digital Micrograph software suggest an approximate composition of $Ti_{30}Ni_{38}Sn_{32}$, which is in broad agreement with the expected Ni-rich stoichiometry, but should only be regarded as indicative without more careful calibration with respect to known standard materials.[38] EDX analysis is more reliable for assessing relative composition and variations across the sample. The variations in Ti, Ni and Sn content within the analyzed region, measured in 1 nm^2 pixels, are inset in Figure 6. These panels all show a similar trend that is consistent with a variation in sample thickness and suggests a homogeneous composition. There are no obvious compositional variations, either across the grain boundary or associated with the features identified as a dislocation network.

DOI: 10.1021/cm5045682
Chem. Mater. 2015, 27, 2449−2459

Figure 7 presents a TEM image of an area straddling a feature within the dislocation network, which appears as a dark

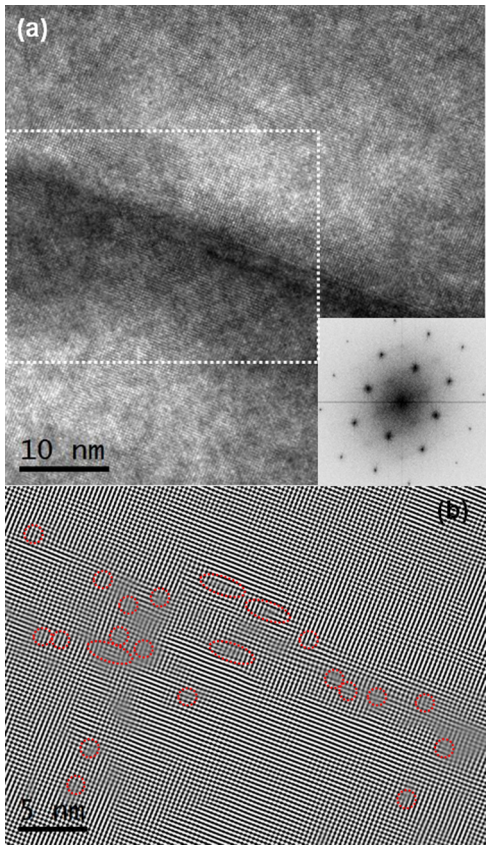

Figure 7. (a) TEM image of a typical linear feature identified as a dislocation network in Figure 5 with (inset) a fast Fourier transform, which does not display obvious splitting of the main spots. (b) Fourier filtered image of the region indicated in a, using the four (001)-type reflections. Weak (gray) contrast indicates regions where the crystal periodicity is interrupted. Circles indicate the approximate position of dislocations in the fringe pattern.

line across the center of Figure 7a. The cross-section was aligned with the electron beam along the (100) direction. A fast Fourier transform of the TEM image is inset to Figure 7a and shows a single set of spots, indicating continuity of the lattice across the field of view: close-ups of the spots do not show splitting that would be consistent with either a local rotation of the lattice or of a change in lattice constant. The four (001)-type spots were used to generate the Fourier-filtered subimage of Figure 7b, which reveals more clearly the principal lattice fringes within the dotted lines of the TEM image. Gray regions where the black-white contrast is weakened are regions where the (001) reflections are weak and typically correspond to the location of dislocations, many of which have been marked by red dashed circles. The dislocations are concentrated within the dark region of the TEM image and we therefore ascribe the contrast in TEM and STEM to arise from local strain.

In previous studies, careful studies of lattice-resolved TEM images has revealed the presence of nanoprecipitates and inclusions,[12,15,32] and the strain from an embedded linear inclusion could account for the linear features seen here in TEM and STEM. On the other hand, subtle variations in thickness and sample angle can give rise to changes in the lattice fringes that need not indicate a change in local composition. We therefore collected a number of spectrum images across a number of the features such as that of Figure 7, using EELS. Typical results are presented in Figure S8 in the Supporting Information, and do not reveal any obvious variations in stoichiometry, oxidation state or local bonding environment. We therefore conclude that the strain fields observed in the TEM images of Figure 7 are inconsistent with compositional variations arising from the presence of inclusions. Thus, the electron microscopy data suggest a rather uniform composition across the field of view and neither direct imaging nor elemental analysis have identified strong phase segregation in the sample. Our estimate of the number density for 50 nm spherical inclusions in $TiNi_{1.05}Sn$ implies an average of one particle in 100 nm^2, which is inconsistent with our observations, suggesting that the excess Ni is more finely dispersed.

Thermoelectric Properties. The temperature dependence of the resistivity ($\rho = 1/\sigma$), Seebeck coefficient (S) and thermoelectric power factor (S^2/ρ) for the three nanocomposite $TiNiM_ySn$ series are shown in Figure 8, while the composition dependence of ρ, S, and S^2/ρ at 300 and 700 K are shown in Figure 9. The thermoelectric properties of the $TiNi_{1+y}Sn$ series were measured for $0 \leq y \leq 1$. The structural analysis has shown that the excess Ni in these phases is distributed over a metal-rich HH phase and a distinct $TiNi_{2-x}Sn$ FH phase. For $y < 0.1$, most of the excess Ni is associated with the HH phase, whereas for $y = 0.1$ the ratio is about 50/50. For $y \geq 0.25$ most of the excess Ni can be found in the distinct $TiNi_{2-x}Sn$ FH phase. However, interestingly, the $\rho(T)$ and $S(T)$ for $y = 0.25$ are still found to be typical of a semiconductor despite the presence of 31 wt % of this metallic phase. This suggests that these larger inclusions are perhaps still well dispersed within the HH matrix and do not form a percolated network. For $y = 0.5$ and 1, metallic behavior is observed. TiNiSn has a large negative $S_{300\ K} = -360\ \mu V\ K^{-1}$ which linearly decreases to $-230\ \mu V\ K^{-1}$ for y = 0.1 (Figure 9a). This is accompanied by a decrease of $\rho_{300\ K}$ from 20 mΩ cm ($y = 0$) to 11 mΩ cm ($y = 0.1$; Figure 9b). The simultaneous decrease of S and ρ is typical of electron doping and leads to a small reduction of S^2/ρ from 0.6 ($y = 0$) to 0.5 mW m^{-1} K^{-1} at 300 K ($y = 0.1$; Figure 9c). The high-temperature S^2/ρ show a decrease from 1.5 to 1.2 mW m^{-1} K^{-1} at 730 K as y is varied from 0 to $y = 0.1$ (Figure 9f). At the highest measured temperatures, similar $\rho = 4-5$ mΩ cm values are observed for $0 \leq y \leq 0.25$ (Figures 8b, 9e). For $y \leq 0.1$, the observed $\rho(T)$ follow a thermally activated behavior and Arrhenius fits were used to extract the thermal bandgap. These fits are shown in Figure S7 in the Supporting Information, and the bandgap values are listed in Table 1. Inspection of the data reveals an almost linear decrease of the bandgap from 0.15 eV ($y = 0$; 2% excess Ni) to 0.08 eV ($y = 0.25$; 8% excess Ni), suggesting that this is linked to the presence of the excess Ni within the HH matrix. The fitted bandgaps are smaller than the 0.2−0.3 eV expected from higher temperature transport measurements[39] and 0.5 eV from first-principles calculations.[40] However, they are in good agreement with data on SPS processed $Ti_{0.5}Zr_{0.5}NiSn$ samples,[41] and signal the presence of in-gap states due to the excess Ni, which reduce the measured effective bandgap.[23,25,42−44]

The $TiNiCo_ySn$ samples consist of a Co-doped HH matrix with Ni-rich regions but do not contain a distinct FH phase. The replacement of Ni ($3d^{10}$) by Co ($3d^9$) is expected to lead to p-type conduction and a transition to positive S values is

DOI: 10.1021/cm5045682
Chem. Mater. 2015, 27, 2449−2459

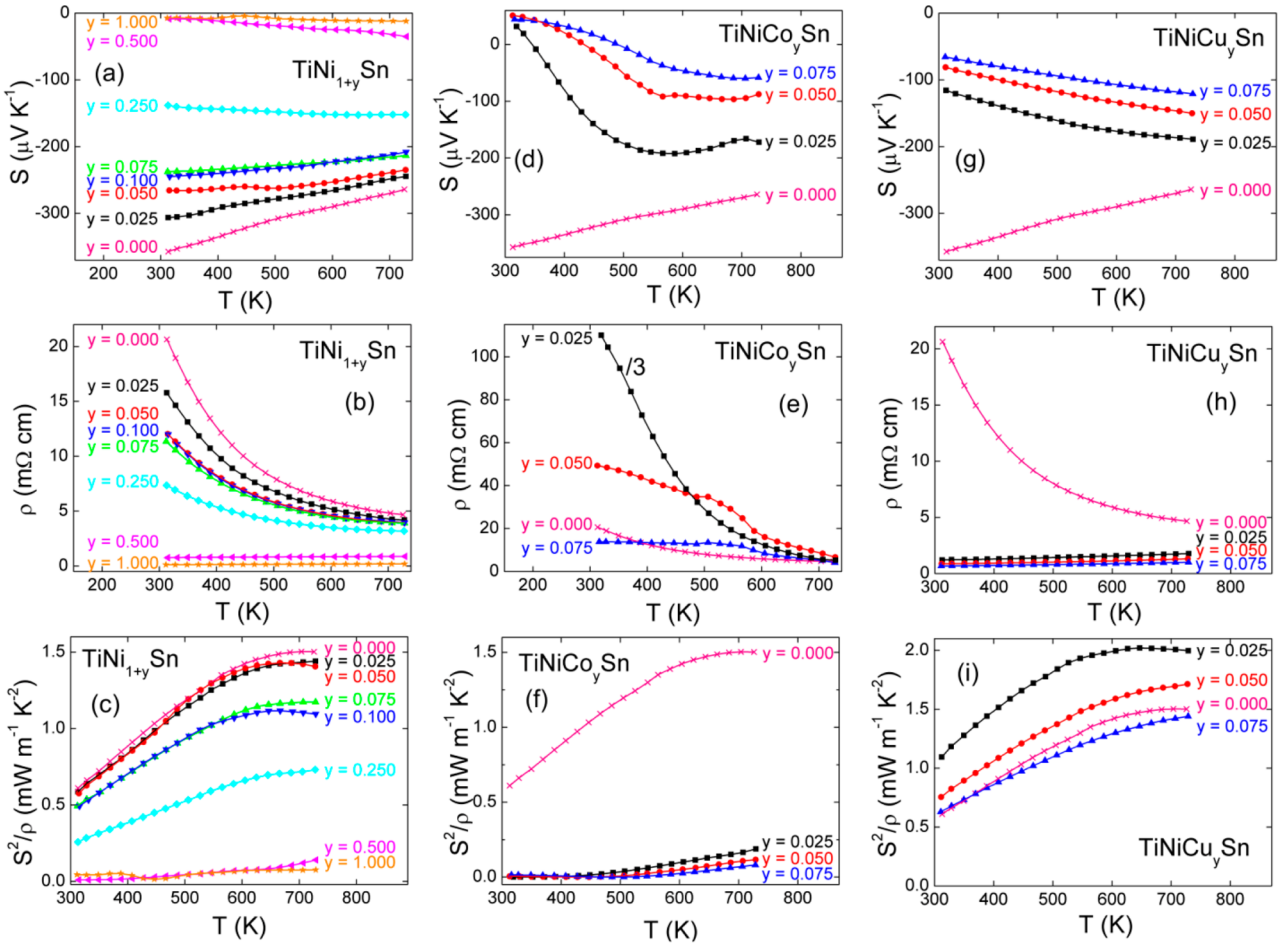

Figure 8. Temperature dependence of the Seebeck coefficient (S), electrical resistivity (ρ), and thermoelectric power factor (S^2/ρ) for the (a–c) $TiNi_{1+y}Sn$, (d–f) $TiNiCo_ySn$, and (g–i) $TiNiCu_ySn$ series. The resistivity of the $TiNiCo_{0.025}Sn$ sample was divided by 3.

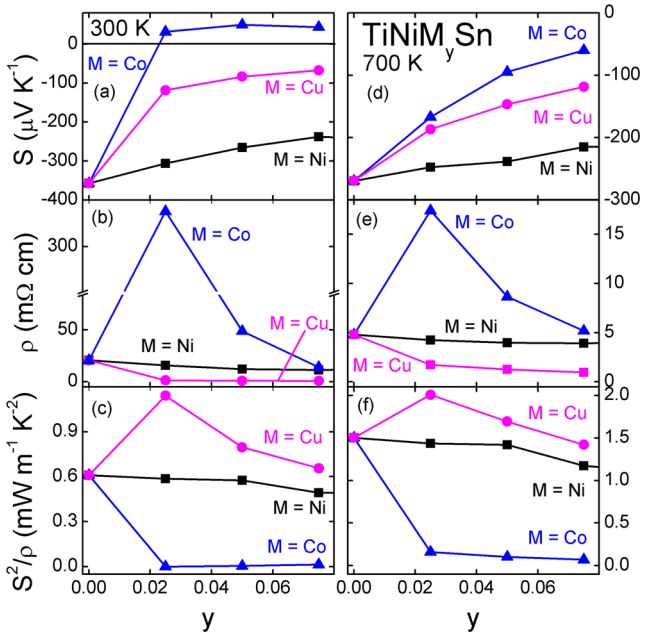

Figure 9. Composition dependence of the Seebeck coefficient (S), electrical resistivity (ρ), and thermoelectric power factor (S^2/ρ) for the $TiNiM_ySn$ (M = Co, Ni and Cu) series at (a–c) 300 and (d–f) 700 K.

indeed observed for $y > 0$. This is accompanied by a rapid increase in ρ for $y = 0.025$, followed by a decrease upon further doping (Figures 8d, e). At first glance this therefore appears to be a typical transition to p-type behavior by hole doping of a semiconductor with the increase in ρ caused by a depletion of charge carriers. However, it is unusual that the magnitude of S does not increase: the maximum $S = +30\ \mu V\ K^{-1}$ occurs at 300 K for $y = 0.025$ and S does not increase for higher Co concentrations (Figures 8d, 9a). Upon heating, a transition to n-type behavior is observed. The transition temperature increases from 345 K ($y = 0.025$) to 430 K ($y = 0.05$) and 490 K ($y = 0.075$). This complex behavior reflects the competition between the hole doped matrix and the in-gap states which are evidenced in the $\rho(T)$ data. Two Arrhenius-type domains are observed, from 300 to 600 K and 600 to 730 K (Figure S7 in the Supporting Information). The crossover at 600 K corresponds to the anomaly in $\rho(T)$ that can be seen in Figure 8e. The >600 K bandgaps are close to those expected from first-principles calculations (0.4–0.5 eV), whereas below 600 K, reduced and decreasing gaps of 0.2 eV ($y = 0.025$), 0.06 eV ($y = 0.05$) and 0.02 eV ($y = 0.075$) are observed. This suggests that above 600 K, the transport is dominated by the excitation of electrons across the intrinsic bandgap. The upturn in $S(T)$ above 600 K also suggest an intrinsic conduction mechanism where electrons and holes are contributing to the transport (Figure 8d). The bandgap below 600 K vanishes for larger amounts of excess metal, which suggests that the

DOI: 10.1021/cm5045682
Chem. Mater. 2015, 27, 2449–2459

transport occurs via an impurity band of in-gap states. This transition to degenerate semiconducting behavior is corroborated by the gradual change to a metal-like $\rho(T)$ below 600 K (Figure 8e). The small magnitude of S means that these composite samples have low S^2/ρ = 0.1−0.2 mW m^{-1} K^{-1} at 730 K (Figure 9f).

The TiNiCu$_y$Sn composites show a remarkable improvement in electronic properties and the segregated Cu ($3d^{10}4s^1$) appears to be an efficient n-type dopant. Both $S(T)$ and $\rho(T)$ decrease in magnitude as y increases and change to a metallic temperature dependence that is characteristic of a degenerate semiconductor (Figure 8g, h). This precludes any reduced bandgaps from being determined and we speculate that the $4s^1$ electron of Cu is transferred into the conduction band of the host matrix, thereby drowning out any contribution from the $3d^{10}$ in-gap states. The value of S^2/ρ is largest for the y = 0.025 sample and reaches values of 1.1 mW m^{-1} K^{-1} at 300 K and 2.0 mW m^{-1} K^{-1} at 700 K, corresponding to a 100 and 33% improvement compared to TiNiSn (Figure 9c, f). The value of S^2/ρ is also improved over the entire temperature range for the y = 0.05 sample and is comparable to TiNiSn for y = 0.075 (Figure 8i). This improvement is comparable to other good n-type dopants and makes these compositions promising for further investigation.

DISCUSSION

There is a large body of experimental and theoretical evidence suggesting that TiNi$_{1+y}$Sn does not support statistical occupancy of the Y2 site, and that instead phase segregation of TiNi$_2$Sn occurs. This strong disfavoring of random Y2 occupation is driven by the energy penalty resulting from disrupting the semiconducting electronic structure of the HH parent material.[23−27] Our XRD and NPD data reveal that the TiNi$_{1+y}$Sn samples consist of a mixture of metal-rich HH and distinct FH phases. The HH lattice expands for $y \leq 0.1$ without any evidence for peak broadening of the Bragg reflections. This suggests that the HH matrix experiences a homogeneous tensile strain, which can only be reconciled with nanosegregation if the FH inclusions are small and numerous enough to disrupt the entire HH lattice. This conclusion is backed up by the microscopy analysis described in Figures 5−7 that did not reveal any obvious segregation, such as the spherical inclusions or larger segregates reported in the literature[10,15] and elemental analysis instead reveals a remarkably homogeneous composition, suggesting a < 2 nm upper limit on the size of any segregated structural phases. Rietveld analysis of NPD data does unambiguously demonstrate that the HH phase is rich in metal and that up to 8% excess Ni can be present. It also reveals a set of distinct TiNi$_{2-x}$Sn FH reflections, which immediately reveals that the particle size of this phase must exceed the coherence length, and likely spans >50−100 nm. The excess Ni is therefore distributed either fairly homogeneously within the HH matrix or well segregated into a distinct FH phase. As expected, the amount of the distinct FH phase increases, and contains the majority of the excess Ni for $y \geq 0.1$. The situation is different for the M = Co and Cu series in the sense that a distinct FH phase is not observed for $y \leq 0.075$, demonstrating (and confirmed by Rietveld analysis of the NPD data) that all excess metal is accommodated within the HH host. For $y \leq 0.075$, a HH lattice expansion without peak broadening is observed indicating a similar well dispersed nature of the excess metal. For $y \geq 0.1$, peak broadening is observed, suggesting that the nanosegregated FH inclusions within the HH matrix are expanding in size. This contrasts with the TiNi$_{1+y}$Sn series where no peak broadening occurs but instead increasing amounts of distinct FH phase are found. It is unclear why a different mode of segregation occurs, and this adds to the interest in these materials. Rietveld analysis of the site occupancies for $y \leq 0.075$ reveals a further difference between the excess Co, Ni and Cu series. Whereas the excess Cu and Ni are found in the nanosegregated FH phase (on the Y2 site), Co prefers to substitute in the matrix (on the Y1 site), and a redistribution of Ni and Co occurs leading to a TiNi$_{1-y}$Co$_y$Sn matrix and nanosegregated TiNi$_{2-y}$Co$_y$Sn. The preference for Co substitution within the HH matrix is consistent with the stronger hybridization of the Co and Ti states that make up the valence and conduction bands, leading to a predicted increase in bandgap and electronic stabilization.[36] Conversely, a reduced bandgap and electronic destabilization may be expected for Cu substitution, which is in keeping with its preference for the segregated phase. We have confirmed the validity and interpretation of the single phase fits by undertaking two-phase fits to the HH reflections. The results of these fits are summarized in Table S3 in the Supporting Information, and give identical sample compositions, thereby confirming the validity of the single phase model used to fit the data. These fits also confirm the site preference of Co for the Y1 site as it was not possible to obtain satisfactory fits using mixtures of TiNiSn and Ti(NiCo)Sn. The only experimental difference between the single and multiphase fits is that it was necessary to allow the displacement parameters (U_{iso}) of the Y site in the FH phase to be refined independent of the Y1 site in the HH matrix. This led to roughly 4× larger U_{iso} values for the segregated phase compared to the values in Tables 1 and 2. The larger displacement parameters could signal structural disorder in the FH segregates due strain arising from the HH matrix, as recently inferred from electron microscopy.[32] A key difference between our samples and other published studies is that our synthesis does not proceed via a melt nor does it include postsynthesis densification using hot-pressing or SPS. This lack of processing may favor a smaller degree of clustering of the excess metal atoms compared to other studies in the literature. The impact of the excess metal on the transport properties is expected to depend sensitively on the nature of the phase segregation in these materials. For $y \leq 0.075$, the excess metal is almost exclusively present within the HH matrix with either none (M = Co, Cu) or only small amounts of distinct FH phase present (M = Ni). One prominent result is the reduction in fitted thermal bandgap, which is consistent with the predicted presence of in-gap states for metal-rich HH nanocomposites.[23] The other is the strikingly different response to excess Ni, Co, and Cu. For M = Ni, the in-gap states appear to result in a larger thermal population of the valence band, leading to a reduced $\rho(T)$ and $^S(T)$, and moderately reduced power factors. The substitution of Co into the matrix leads to hole doping, while the displacement of Ni leads to in-gap states similar to TiNi$_{1+y}$Sn. The interplay between the hole doping and the in-gap states leads to a complex response of $\rho(T)$ and $S(T)$. It would be of considerable interest to compare these results to hole-doped TiNi$_{1-x}$Co$_x$Sn samples prepared in an analogous manner. The ZrNiCo$_y$Sn composites in the literature show a different thermoelectric response with clear p-type semiconducting behavior over the entire measured temperature range.[31] The TiNiCu$_y$Sn series is of possible interest for obtaining good thermoelectric performance. The Cu $4s^1$ electron appears to become delocalized in the HH matrix and

DOI: 10.1021/cm5045682
Chem. Mater. 2015, 27, 2449−2459

metal-like electrical conduction and substantially improved power factors are observed. The changes in $S(T)$ and $\rho(T)$ for y = 0.025 are comparable to those observed for 2% Sb substitution in $Ti_{0.5}Zr_{0.5}NiSn$ prepared by solid state reaction,[35] suggesting that all of the $4s^1$ electrons transfer to the HH matrix. If these results can be transferred to dense $TiNiCu_ySn$ samples, $ZT \sim 1$ may be achievable.

CONCLUSIONS

The metal distributions and thermoelectric properties of $TiNiM_ySn$ (M = Co, Ni, Cu) nanocomposites have been investigated. The Ni and Cu series consist of a matrix of a TiNiSn with nanosegregated $TiNi_2Sn$ and $TiNi_{1+d}Cu_{1-d}Sn$, respectively. For the Co series, a composite consisting of a $TiNi_{1-y}Co_ySn$ matrix and nanosegregated $TiNi_{2-y}Co_ySn$ is observed. These results broaden the range of segregated FH phases that could be used to enhance HH thermoelectric performance. The Cu series shows a substantially improved thermoelectric power factor and is of interest for further investigation.

ASSOCIATED CONTENT

Supporting Information

Tables with crystallographic information, X-ray powder diffraction patterns for all $TiNiM_ySn$ compositions, and Rietveld fits to neutron powder diffraction data for the $TiNiM_ySn$ and $TNi_{1-z}Sn$ series. Scanning electron microscopy images and elemental maps for TiNiSn. TEM and EELS data for $TiNi_{1.05}Sn$. Temperature dependence of the Seebeck coefficient and electrical resistivity for the $TNi_{1-z}Sn$ samples. Arrhenius fits to the resistivity data for the $TiNiM_ySn$ (M = Co and Ni) samples. This material is available free of charge via the Internet at http://pubs.acs.org.

AUTHOR INFORMATION

Corresponding Author

*E-mail: j.w.g.bos@hw.ac.uk.

Notes

The authors declare no competing financial interest.

ACKNOWLEDGMENTS

We acknowledge the EPSRC (EP/J000884/1 and EP/K036408/1) and Royal Society for support and the STFC for facility time at the ISIS Rutherford-Appleton Laboratory.

REFERENCES

(1) Zebarjadi, M.; Esfarjani, K.; Dresselhaus, M. S.; Ren, Z. F.; Chen, G. *Energy Environ. Sci.* **2012**, *5*, 5147.
(2) Minnich, A. J.; Dresselhaus, M. S.; Ren, Z. F.; Chen, G. *Energy Environ. Sci.* **2009**, *2*, 466.
(3) Snyder, G. J.; Toberer, E. S. *Nat. Mater.* **2008**, *7*, 105.
(4) Chen, S.; Ren, Z. F. *Mater. Today* **2013**, *16*, 387.
(5) Xie, W.; Weidenkaff, A.; Tang, X.; Zhang, Q.; Poon, J.; Tritt, T. *Nanomaterials* **2012**, *2*, 379.
(6) Bos, J.-W. G.; Downie, R. A. *J. Phys.: Condens. Matter* **2014**, *26*, 433201.
(7) Kimura, Y.; Asami, C.; Chai, Y.-W.; Mishima, Y.; Nie, J. F.; Morton, A. In *7th Pacific Rim International Conference on Advanced Materials and Processing (PRICM 7)*; Cairns, Australia, Aug 2−6, 2010 ; Materials Australia: Parkville, Victoria, Australia, 2010; Vol. *654*−*656*, p 2795.
(8) Hazama, H.; Matsubara, M.; Asahi, R.; Takeuchi, T. *J. Appl. Phys.* **2011**, *110*, 063710.
(9) Makongo, J. P. A.; Misra, D. K.; Salvador, J. R.; Takas, N. J.; Wang, G.; Shabetai, M. R.; Pant, A.; Paudel, P.; Uher, C.; Stokes, K. L.; Poudeu, P. F. P. *J. Solid State Chem.* **2011**, *184*, 2948.
(10) Makongo, J. P. A.; Misra, D. K.; Zhou, X.; Pant, A.; Shabetai, M. R.; Su, X.; Uher, C.; Stokes, K. L.; Poudeu, P. F. P. *J. Am. Chem. Soc.* **2011**, *133*, 18843.
(11) Hazama, H.; Matsubara, M.; Asahi, R. *J. Electron. Mater.* **2012**, *41*, 1730.
(12) Chai, Y. W.; Kimura, Y. *Appl. Phys. Lett.* **2012**, *100*, 033114.
(13) Xie, H. H.; Mi, J. L.; Hu, L. P.; Lock, N.; Chirstensen, M.; Fu, C. G.; Iversen, B. B.; Zhao, X. B.; Zhu, T. J. *CrystEngComm* **2012**, *14*, 4467.
(14) Douglas, J. E.; Birkel, C. S.; Miao, M.-S.; Torbet, C. J.; Stucky, G. D.; Pollock, T. M.; Seshadri, R. *Appl. Phys. Lett.* **2012**, *101*, 183902.
(15) Chai, Y. W.; Kimura, Y. *Acta Mater.* **2013**, *61*, 6684.
(16) Birkel, C. S.; Douglas, J. E.; Lettiere, B. R.; Seward, G.; Verma, N.; Zhang, Y. C.; Pollock, T. M.; Seshadri, R.; Stucky, G. D. *Phys. Chem. Chem. Phys.* **2013**, *15*, 6990.
(17) Downie, R. A.; MacLaren, D. A.; Smith, R. I.; Bos, J. W. G. *Chem. Commun.* **2013**, *49*, 4184.
(18) Liu, Y.; Sahoo, P.; Makongo, J. P. A.; Zhou, X.; Kim, S.-J.; Chi, H.; Uher, C.; Pan, X.; Poudeu, P. F. P. *J. Am. Chem. Soc.* **2013**, *135*, 7486.
(19) Sahoo, P.; Liu, Y.; Makongo, J. P. A.; Su, X.-L.; Kim, S. J.; Takas, N.; Chi, H.; Uher, C.; Pan, X.; Poudeu, P. F. P. *Nanoscale* **2013**, *5*, 9419.
(20) Douglas, J. E.; Birkel, C. S.; Verma, N.; Miller, V. M.; Miao, M.-S.; Stucky, G. D.; Pollock, T. M.; Seshadri, R. *J. Appl. Phys.* **2014**, *115*, 043720.
(21) Xie, H.; Wang, H.; Fu, C.; Liu, Y.; Snyder, G. J.; Zhao, X.; Zhu, T. *Sci. Rep.* **2014**, *4*, 6888.
(22) Birkel, C. S.; Douglas, J. E.; Lettiere, B. R.; Seward, G.; Verma, N.; Zhang, Y.; Pollock, T. M.; Seshadri, R.; Stucky, G. D. *Phys. Chem. Chem. Phys.* **2013**, *15*, 6990.
(23) Do, D. T.; Mahanti, S. D.; Pulikkoti, J. J. *J. Phys.: Condens. Matter* **2014**, *26*, 275501.
(24) Kirievsky, K.; Shlimovich, M.; Fuks, D.; Gelbstein, Y. *Phys. Chem. Chem. Phys.* **2014**, *16*, 20023.
(25) Douglas, J. E.; Chater, P. A.; Brown, C. M.; Pollock, T. M.; Seshadri, R. *J. Appl. Phys.* **2014**, *116*, 163514.
(26) Kirievsky, K.; Gelbstein, Y.; Fuks, D. *J. Solid State Chem.* **2013**, *203*, 247.
(27) Larson, P.; Mahanti, S. D.; Kanatzidis, M. G. *Phys. Rev. B* **2000**, *62*, 12754.
(28) Stadnyk, Y. V.; Skolozdra, R. V. *Inorg. Mater.* **1991**, *27*, 1884.
(29) Romaka, V. V.; Rogl, P.; Romaka, L.; Stadnyk, Y.; Melnychenko, N.; Grytsiv, A.; Falmbigl, M.; Skryabina, N. *J. Solid State Chem.* **2013**, *197*, 103.
(30) Quarez, E.; Hsu, K.-F.; Pcionek, R.; Frangis, N.; Polychroniadis, E. K.; Kanatzidis, M. G. *J. Am. Chem. Soc.* **2005**, *127*, 9177.
(31) Kimura, Y.; Tanoguchi, T.; Kita, T. *Acta Mater.* **2010**, *58*, 4354.
(32) Chai, Y. W.; Yoshioka, K.; Kimura, Y. *Scr. Mater.* **2014**, *83*, 13.
(33) Toby, B. H. *J. Appl. Crystallogr.* **2001**, *34*, 210.
(34) Larson, A. C.; Dreele, R. B. V. *Los Alamos National Laboratory Report LAUR 86-748: General Structure Analysis*; Los Alamos National Laboratory: Los Alamos, NM, 1994.
(35) Downie, R. A.; MacLaren, D. A.; Bos, J. W. G. *J. Mater. Chem., A* **2014**, *2*, 6107.
(36) Graf, T.; Felser, C.; Parkin, S. S. P. *Prog. Solid State Chem.* **2011**, *39*, 1.
(37) Gelbstein, Y.; Tal, N.; Yarmek, A.; Rosenberg, Y.; Dariel, M. P.; Ouardi, S.; Balke, B.; Felser, C.; Kohne, M. *J. Mater. Res.* **2011**, *26*, 1919.
(38) Willams, D. B.; Carter, C. B. *Transmission Electron Microscopy*; Springer: New York, 1996.
(39) Simonson, J. W.; Poon, S. J. *J. Phys.: Condens. Matter* **2008**, *20*, 255220.
(40) Ogut, S.; Rabe, K. *Phys. Rev. B* **1995**, *51*, 10443.

DOI: 10.1021/cm5045682
Chem. Mater. 2015, 27, 2449−2459

(41) Downie, R. A.; Popuri, S.; Ning, H.; Reece, M. J.; Bos, J.-W. G. *Materials* **2014**, *7*, 7093.
(42) Miyamoto, K.; Kimura, A.; Sakamoto, K.; Ye, M.; Cui, Y.; Shimada, K.; Namatame, H.; Taniguchi, M.; Fujimori, S. I.; Saitoh, Y.; Ikenaga, E.; Kobayashi, K.; Tadano, J.; Kanomata, T. *Appl. Phys. Express* **2008**, *1*, 081901.
(43) Ouardi, S.; Fecher, G. H.; Felser, C.; Blum, C. G. F.; Bombor, D.; Hess, C.; Wurmehl, S.; Buchner, B.; Ikenaga, E. *Appl. Phys. Lett.* **2011**, *99*, 152112.
(44) Schmitt, J.; Gibbs, Z. M.; Snyder, G. J.; Felser, C. *Mater. Horiz.* **2015**, *2*, 68−75.

DOI: 10.1021/cm5045682
Chem. Mater. 2015, 27, 2449−2459